

Tunable Magnetic and Topological Phases in EuMnXBi₂ (X=Mn, Fe, Co, Zn) Pnictides

Deep Sagar^a, Abhishek Sharma^b and Arti Kashyap^{a,*}

^aIndian Institute of Technology, School of Physical Sciences, Mandi, 175005, Himachal Pradesh, India

^bIndian Institute of Technology, School of Computing and Electrical Engineering, Mandi, 175005, Himachal Pradesh, India

ARTICLE INFO

Keywords:

Density Functional Theory
Pnictide
Topological materials
Magnetic Ordering

ABSTRACT

We present a comprehensive density functional theory (DFT) study of the electronic, magnetic, and topological properties of the layered pnictides EuMnXBi₂ (X = Mn, Fe, Co, Zn), focusing in particular on the relatively unexplored Bi-based member of the EuMn₂X₂ family. Unlike the well-studied As-, Sb-, and P-based analogues, we show that EuMn₂Bi₂ stabilizes in a C-type antiferromagnetic ground state with a narrow-gap semiconducting character. Inclusion of spin-orbit coupling (SOC) drives a transition from this trivial antiferromagnetic semiconductor to a Weyl semimetal hosting four symmetry-related Weyl points and robust Fermi arc states. Systematic substitution of Mn with Fe, Co, and Zn further reveals a tunable sequence of magnetic ground states: Fe and Co induce ferrimagnetism with semimetallic behavior, while Zn stabilizes a ferromagnetic semimetal with a large net moment. These findings establish Bi-based EuMnXBi₂ pnictides as a versatile platform where magnetic exchange interactions and band topology can be engineered through SOC and chemical substitution. The complex interplay of magnetic interactions and topological effects in the proposed bulk and doped pnictides opens a promising avenue to explore a wide range of electronic and magnetic phenomena. In particular, this study demonstrates that EuMn₂Bi₂ hosts tunable magnetic and topological phases driven by electron correlations, chemical substitution, and spin-orbit coupling.

1. Introduction

Layered pnictides with the general formula AB_2P_2 (A = rare-earth or alkaline-earth metal, T = transition metal, P = pnictogen) have long served as a rich platform to study correlated electronic states, magnetism, and emergent topological phases. Compounds crystallizing in the tetragonal ThCr₂Si₂-type [1, 2] and trigonal CaAl₂Si₂-type [3] structures exhibit diverse quantum phenomena, including high- T_c superconductivity, spin-density-wave transitions, and magnetically driven metal-insulator transitions. The ThCr₂Si₂-type iron pnictides, such as EuFe₂As₂, have been extensively explored for their pressure- and doping-induced superconductivity [4, 5]. The CaAl₂Si₂-type structure is mainly driven by its topological and thermoelectric properties. For example, both electrons and holes contribute to the electrical transport properties of the prototype material CaAl₂Si₂ [6, 7]. Within the CaAl₂Si₂-type structure, the transition metal can have fully occupied (d^{10}), partially filled (d^5), or unoccupied (d^0) d orbitals. In contrast, in the ThCr₂Si₂-type structure, there is no such preference for the transition metal [8].

Recently, researchers have turned their attention towards layered trigonal Mn-based pnictides. This shift arises due to the challenges associated with Fe-based pnictides, which are high- T_c superconductors but face significant difficulties in achieving the desired transition temperatures (T_c 's) [9]. Most Mn-based layered pnictides exhibit the properties of antiferromagnetic insulators [9]. The induction of an electronic delocalization transition (EDT) [10] through doping

or applying pressure could potentially transform them into a strongly correlated metallic state, which is a crucial precursor for unconventional superconductivity. However, compounds such as LaMnPO [11] and BaMn₂As₂ [12] remain insulators even after heavy doping. Consequently, despite the EDT induced by doping or pressure, superconductivity has not been observed in these cases.

The Mn-based AB_2P_2 pnictides typically stabilize in robust antiferromagnetic (AFM) insulating states [11], and attempts to induce metallicity or superconductivity via chemical substitution or external pressure have largely been unsuccessful [11, 13]. Among the EuMn₂X₂ (X = P, As, and Sb) family, various AFM transitions and semiconducting behaviors have been reported. These pnictide compounds were first proposed in 1979 by R. Ruhl *et al.* [3], who introduced rare-earth and transition-metal Mn-based pnictides crystallizing in either anti-Ce₂O₂S or CaAl₂Si₂-type structures. Since then, many studies have investigated the structural and magnetic properties of the EuMn₂X₂ series. Anand *et al.* [8] found that EuMn₂As₂ possesses an insulating ground state with an activation energy of around 53 meV. Furthermore, it demonstrates antiferromagnetic (AFM) ordering of Eu²⁺ moments with $S = 7/2$ at both 15 K and 5 K, while the Mn²⁺ moments exhibit AFM ordering with $S = 5/2$ at 142 K. When doped with 4% and 7% potassium (K) for Eu in Eu_{1-x}K_xMn₂As₂, the material transitions to a metallic ground state. Dahal *et al.* [13] reported that EuMn₂As₂ displays two distinct AFM transitions on $T = 135$ K and 14.4 K. The AFM behavior of EuMn₂P₂ with a Néel temperature around 16.5 K, was discovered by Payne *et al.* [14]. Between 300 K and 120 K, this compound exhibits semiconducting behavior with an activation energy of 38.9 meV. Berry *et al.* [15] discovered that EuMn₂P₂ remains an AFM insulator

*Arti Kashyap

 arti@iitmandi.ac.in (A. Kashyap)

at all temperatures, undergoing a phase transition at $T = 20$ K for Eu long-range AFM ordering and at $T = 130$ K for Mn long-range AFM ordering. With an indirect band gap of roughly 450 meV for Mn magnetic ordering and Eu in the core, the compound also demonstrates semiconducting behavior. However, considering the Eu magnetic order, the indirect gap significantly decreases to around 0.29 eV. Schellenberg *et al.* [16] reported that the magnetic moment of EuMn_2Sb_2 is zero, and it displays AFM behavior with the magnetic moments of Eu^{2+} and Mn^{2+} being $7.94 \mu_B$ and $5.92 \mu_B$, respectively. While As-, Sb-, and P-based Eu–Mn pnictides are well studied, little attention has been paid to the Bi-based system. Karl *et al.* [17] reported that all EuMn_2X_2 ($\text{X} = \text{As, Sb, Bi, P}$) compounds may be isostructural and possibly semiconducting. Very recently, Khatri *et al.* [18] predicted magnetization in several Mn-based pnictide compounds using machine learning techniques and reported the stability of these, including Bi-based pnictides, based on the formation-energy criterion. However, their Bi-based analogue EuMn_2Bi_2 has received little attention, despite theoretical predictions based on machine learning techniques indicating its stability according to the formation-energy criterion [18]. Recently, [19] predicted from first-principle calculations that EuMn_2Bi_2 boasts a C_0 -AFM ground state with a very small band gap and several nearly degenerate magnetic states exhibiting Dirac/Weyl semimetal and topological insulating behavior. This establishes EuMn_2Bi_2 as a promising platform for magnetic topological phases. However, the roles of spin-orbit coupling (SOC), magnetic exchange interactions, and transition-metal substitution in stabilizing these phases remain unexplored.

This gap is particularly significant because bismuth contributes strong $6p$ spin-orbit coupling (SOC), which can drive band inversions and topological phase transitions when combined with broken time-reversal symmetry from magnetic order. Such conditions are known to stabilize magnetic Weyl semimetal (WSM) phases in related systems such as EuCd_2Bi_2 and $\text{Co}_3\text{Sn}_2\text{S}_2$ [20, 21]. Uncovering similar behavior in EuMn_2Bi_2 could provide a rare platform to tune magnetism and topology within a single material system.

Here, we present a comprehensive density functional theory (DFT) study of EuMn_2Bi_2 and its doped analogues EuMnXBi_2 ($\text{X} = \text{Fe, Co, Zn}$). Our calculations reveal that pristine EuMn_2Bi_2 stabilizes in a C-type AFM ground state and undergoes an SOC-driven transition to a WSM hosting four symmetry-related Weyl points and topological Fermi arc surface states. Substituting Mn with Fe or Co induces ferrimagnetism with semimetallic behavior, while Zn stabilizes a ferromagnetic semimetal with a large net moment.

These results establish EuMnXBi_2 as a tunable platform where magnetic exchange interactions and band topology can be engineered via chemical substitution and SOC, providing new opportunities for realizing correlated magnetic topological phases relevant to next-generation spintronic devices.

2. Computational Methods

First-principle calculations were performed using the VASP package [22, 23] within the framework of density functional theory (DFT) and the projector-augmented wave (PAW) method. The exchange-correlation energy was treated using the generalized gradient approximation (GGA) of Perdew, Burke, and Ernzerhof (PBE) [24]. A plane-wave energy cutoff of 520 eV and a Gaussian smearing width of 0.05 eV were used, ensuring total-energy convergence within 1 meV per formula unit. Structural relaxations employed a Monkhorst-Pack $5 \times 5 \times 3$ k -point mesh, while electronic density of states (DOS) calculations used a denser $10 \times 10 \times 6$ mesh [25].

Strongly correlated Eu-4*f* and Mn-3*d* states were treated using the GGA+*U* scheme [26, 27] with effective Hubbard parameters $U_{\text{eff}} = U - J$ of 6.32 eV for Eu and 4.16 eV for Mn, determined from the linear response method [28]. Additional calculations were also carried out with $U_{\text{eff}} = 5$ eV for comparison [15]. Spin-orbit coupling (SOC) was included self-consistently, as it is expected to significantly influence the band topology of these Bi-based compounds [29].

Topological properties of EuMn_2Bi_2 , including Berry curvature, Weyl points, and surface states, were evaluated using WANNIER90 [30] to construct maximally localized Wannier functions (MLWFs) [31], and WANNIER-TOOLS [32] to compute Berry curvature distribution, surface spectral functions, and Fermi arcs from the resulting tight-binding Hamiltonian.

Magnetic exchange interactions were modeled using the Heisenberg Hamiltonian

$$H = - \sum_{i,j} J_{ij} \mathbf{S}_i \cdot \mathbf{S}_j, \quad (1)$$

where J_{ij} represents the effective exchange coupling between spins i and j . Exchange parameter was extracted from the total-energy difference $\Delta E = E_{\text{AFM}} - E_{\text{FM}}$ as

$$J_{\text{eff}} = \frac{\Delta E}{2N Z S^2}, \quad (2)$$

where N is the number of magnetic atoms, Z the number of nearest neighbors, and S the spin quantum number. The Curie temperature was then estimated using the molecular-field approximation:

$$T_c = \frac{2}{3} \frac{ZJS(S+1)}{k_B}, \quad (3)$$

where k_B is the Boltzmann constant [33, 34, 35, 36].

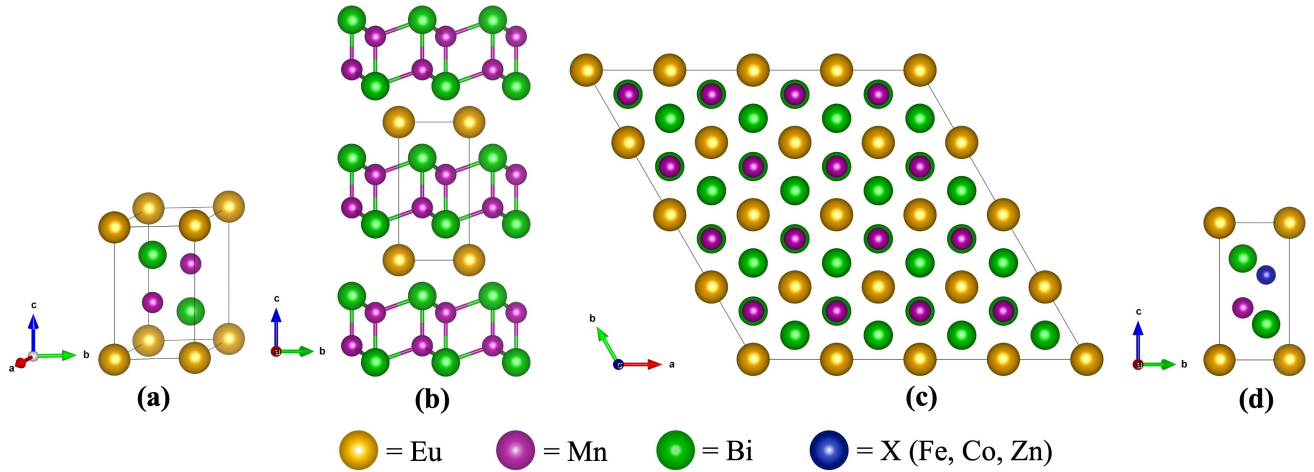


Figure 1: Crystal structure of EuMn₂Bi₂, EuMnXBi₂ (X = Fe, Co, and Zn), and arrangement of Eu, Mn, and Bi atoms. (a) Crystal structure of EuMn₂Bi₂, (b) the [MnBi₂]₂⁻ networks and Mn–Bi layers. (c) top view showing triangular Eu and honeycomb Mn sublattices. (d) Unit cell of Fe, Co, and Zn replacing X in EuMnXBi₂. yellow = Europium (Eu), purple = Manganese (Mn), and green = Bismuth (Bi), and blue = Iron (Fe), Cobalt (Co), and Zinc (Zn).

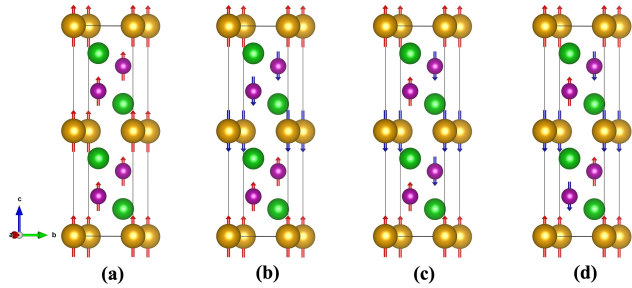


Figure 2: Magnetic crystal structure of the EuMn₂Bi₂ supercell (1 x 1 x 2) for Ferromagnetic and three types of anti-ferromagnetic magnetic configurations. (a) FM. (b) A-AFM. (c) C-AFM. (d) G -AFM.

3. Results and discussion

3.1. Crystal structure optimization and magnetic ordering

EuMn₂Bi₂ crystallizes in the trigonal CaAl₂Si₂-type structure (space group $P\bar{3}1$, No. 164). Eu occupies the 1a (0,0,0) site, while Mn and Bi occupy 2d (1/3,2/3,0.62) and (1/3,2/3,0.62) sites, respectively [Fig. 1(a)]. Fig. 1(b) illustrates the EuMn₂Bi₂ structure, highlighting the [MnBi₂]₂⁻ networks and Mn–Bi layers, whereas Fig. 1(c) shows the hexagonal arrangement of Eu, Mn, and Bi atoms in the EuMn₂Bi₂ structure. The Eu atoms form triangular-lattice layers, while the Mn atoms form a corrugated honeycomb-like lattice. The unit cell for the substituted system is presented in Fig. 1(d).

Relaxed lattice constants are $a = 4.618 \text{ \AA}$ and $c = 7.884 \text{ \AA}$ ($V = 145.64 \text{ \AA}^3$), consistent with other EuMn₂X₂

Table 1
Calculated lattice parameters of EuMn₂Bi₂ and doped compounds.

Compound	a (Å)	c (Å)	c/a	V (Å ³)
EuMn ₂ Bi ₂	4.618	7.884	1.71	145.64
EuMnFeBi ₂	4.384	8.109	1.85	134.99
EuMnCoBi ₂	4.238	8.320	1.96	129.46
EuMnZnBi ₂	4.684	7.729	1.65	146.91

pnictides [8, 14, 15, 16]. Doped EuMnXBi₂ (X=Fe, Co, Zn) compounds exhibits comparable equilibrium volume to pristine EuMn₂Bi₂, indicating their structural stability. The fully relaxed lattice parameters of EuMn₂Bi₂ and its doped analogues (obtained by substituting one Mn atom in the EuMn₂Bi₂ unit cell) are summarized in Table 1.

For all the systems, EuMnXBi₂ (X = Mn, Fe, and Co), the Eu, Mn, and X spin moments were considered in both ferromagnetic (FM) and antiferromagnetic (AFM) arrangements. In the FM configuration, the spin orientations of the Eu, Mn, and X atoms are aligned z -axis, whereas in the AFM configuration, three distinct spin arrangements emerge: A-AFM, C-AFM, and G-AFM. In all AFM configurations, the Eu spin moments are orientated along the z -axis and cancel each other between the top and bottom planes. In the EuMn₂Bi₂ structure, the A-AFM configuration is characterized by Mn spin moments that cancel each other between the top and bottom planes, as shown in Fig. 2(b). The C-AFM configuration is characterized by Mn spin moments that cancel each other over parallel planes, as shown in Fig. 2(c). The G-AFM configuration is characterized by Mn spin moments that cancel each other both between the top and bottom planes and between parallel planes, as shown in

Fig. 2(d). In EuMnXBi_2 (X = Fe, Co), the spin configuration is consistent in both the FM state and the three AFM configurations, whereas in EuMnZnBi_2 , the FM and A-AFM configurations are exits. Due to the extremely low magnetic moments of Bi and Zn, their spins were not considered in our calculations.

3.2. Electronic and magnetic properties of antiferromagnetic EuMn_2Bi_2

The total energy calculations for both the ferromagnetic (FM) and various antiferromagnetic (AFM) configurations were performed within GGA and GGA+ U using different values of the Hubbard U , and the results are summarized in Table 2. To provide a better description of the partially filled and strongly correlated electronic states in the highly localized rare-earth Eu-4f and transition-metal Mn-3d orbitals, the GGA+ U method was adopted [26, 27]. We used two different values of the effective Hubbard parameter, $U_{\text{eff}} = U - J$, for the half-filled Eu- f orbital and the partially filled Mn- d orbital, where U is the on-site Coulomb correlation and J is Hund's exchange. First, we employed $U_{\text{eff}} = 5$ eV for both Eu and Mn, as reported in Ref. [15]. Second, we used U_{eff} values of 6.32 eV and 4.16 eV for Eu and Mn, respectively, which we calculated *ab-initio* using the Linear Response (LR) approach [28]. This approach has proven to be more reliable than the empirical approach [37, 38], thereby avoiding the empiricism and ambiguities common in many DFT+ U studies. Notably, the *ab-initio* value of $U_{\text{eff}} = 6.32$ eV obtained for Eu closely matches the $U_{\text{eff}} = 6.3$ eV value employed in EuCd_2As_2 [39].

In GGA, the lowest energy state of EuMn_2Bi_2 is found to be the G-AFM configuration, with the FM and A-AFM states lying much higher in energy compared to the C-AFM and G-AFM states. The lowest energy state within GGA+ U ($U_{\text{eff}} = 5$ eV for both Eu and Mn) is also G-AFM; however, the C-AFM state is nearly degenerate in energy. When the values of U_{eff} are 6.32 eV and 4.16 eV for Eu and Mn, respectively, the lowest energies state of the C-AFM and G-AFM states becomes nearly identical, as shown in Table 2. This indicates that C-AFM and G-AFM are equi-energetic magnetic states, both lying lower in energy than the other magnetic configurations. Consequently, detailed calculations were carried out only for the C-AFM state. The extremely small energy separation between the C-AFM and G-AFM states indicates that EuMn_2Bi_2 resides very close to a magnetic phase boundary. Such magnetic near-degeneracy makes the system highly responsive to external perturbations, including chemical substitution, lattice strain, hydrostatic pressure, and applied magnetic fields. Even modest perturbations may therefore alter the balance between the two AFM configurations and potentially drive a transition between C-AFM and G-AFM order. Similar sensitivity to external tuning has been widely reported in correlated and frustrated magnets hosting nearly degenerate spin states [40,

Table 2

Magnetic configurations of EuMn_2Bi_2 calculated within GGA, GGA+ U ($U_{\text{Eu}} = 5.00$ eV, $U_{\text{Mn}} = 5.00$ eV) and GGA+ U ($U_{\text{Eu}} = 6.32$ eV, $U_{\text{Mn}} = 4.16$ eV). Listed are the total energy difference $\Delta E = E_{\text{AFM}} - E_{\text{FM}}$ (eV/f.u.), band gap E_g (eV), and site-projected magnetic moments (μ_B).

	GGA	GGA+U	
U_{eff} (Eu)	—	5.00	6.32
U_{eff} (Mn)	—	5.00	4.16
FM	-72.050	-65.271	-65.920
A-AFM	-72.060	-65.333	-65.981
C-AFM	-73.030	-65.588	-66.296
G-AFM	-73.043	-65.596	-66.290
ΔE	-0.993	-0.320	-0.370
E_g	0.0	0.122	0.258
μ_{Eu}	6.81	6.96	6.98
μ_{Mn}	3.94	4.62	4.55

41, 42, 43]. In EuMn_2Bi_2 , this is particularly relevant because the G-AFM state has been predicted to host a Dirac semimetal phase [19], while our LR-derived Hubbard U values stabilize the C-AFM state, which lies 6 meV lower in energy than G-AFM. The effect of this near-degeneracy becomes even more evident upon doping. The substitution of Fe/Co/Zn perturbs the Mn-Bi-Mn super-exchange pathways and modifies the local electronic environment Mn-3d, thus lifting the intrinsic energy balance and robustly stabilizing the C-AFM order, further details are provided in Section 3.4.

Using GGA+ U , the energy difference between AFM and FM configurations is -0.37 eV. Our system gives $J_{\text{eff}} = -1.64$ meV and -1.1 meV, indicating strong exchange interactions $J_{\text{Mn-Mn}}$ and $J_{\text{Eu-Mn}}$ [44], whereas the exchange interaction $J_{\text{Eu-Eu}}$ is much weaker, with a value of -0.08 meV. The Curie temperature T_c was estimated using the molecular-field approximation [Eq.(3)], yielding $T_c = 278.5$ K. This value is known to systematically overestimate ordering temperature because spin fluctuations are neglected [45, 46].

Further, the magnetic properties of EuMn_2Bi_2 were investigated using both GGA and GGA+ U methods. Experimental and theoretical data for Eu^{2+} ions indicate magnetic moments of 7.89 μ_B /Eu and 7 μ_B /Eu, respectively, with spin $S = 7/2$, exhibiting AFM ordering [8]. For Mn^{2+} ions, the magnetic moment is reported to be 5.92 μ_B /Mn, also exhibiting AFM ordering [16]. In our study, the calculated magnetic moments for Eu^{2+} ions are $\pm 6.811 \mu_B$ /Eu, $\pm 6.964 \mu_B$ /Eu, and $\pm 6.982 \mu_B$ /Eu in the GGA and GGA+ U methods, respectively. For Mn^{2+} ions, the magnetic moments are $\pm 3.946 \mu_B$ /Mn, $\pm 4.619 \mu_B$ /Mn, and $\pm 4.554 \mu_B$ /Mn in the GGA and GGA+ U methods, respectively, as shown in Table 2. The total magnetic moment of EuMn_2Bi_2 is found to be zero, consistent with AFM magnetic ordering.

As heavy orbitals such as Eu-4f, Mn-3d, and Bi-6p are present in this compound, the effect of spin-orbit coupling (SOC) is significant, and SOC plays an important role in

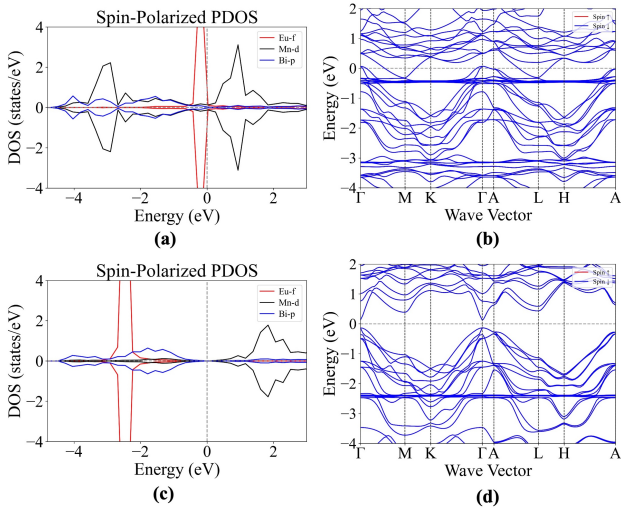


Figure 3: Spin-polarized projected density of state (PDOS) and electronic band structure for the magnetic ground state of EuMn_2Bi_2 in the G-AFM magnetic ground state (a)-(b) calculated within GGA. (c)-(d) calculated within GGA+U with $U_{\text{eff}} = 6.32$ eV for Eu and 4.16 eV for Mn.

calculating the electronic properties of the material [29]. Therefore, SOC was included in the electronic structure calculations. We observe that the GGA+U+SOC results are superior when compared to those obtained from GGA and GGA+U, since the ground-state energy obtained with SOC is lower than that with GGA+U, and the exchange energy is also reduced compared to GGA and GGA+U, as shown in Table 2.

Fig. 3(a) displays the Spin-polarized projected density of state (PDOS) for the G-AFM configuration within GGA. In this PDOS plot, the Eu- f ($4f^7$) and Mn- d ($3d^5$) states are highly localized at the Fermi level (E_F), with small localized Bi- p states intersecting E_F . Moreover, the Eu- d , Mn- s , and Bi- s states are highly delocalized below E_F . From the PDOS plots in GGA, it is evident that the G-AFM magnetic configuration exhibits metallic behavior. However, the GGA+U method with $U_{\text{eff}} = 5$ eV and 6.32 eV for the Eu- f state, and $U_{\text{eff}} = 5$ eV and 4.16 eV for the Mn- d state across FM and all AFM magnetic configurations, opens up a band gap in the DOS. The ground-state energy calculated using U obtained from the LR approach [28] is lower than that calculated using U values taken from the literature, and the resulting band gap is also larger, as shown in Table 2. Therefore, we focus our discussion on the results obtained with $U = 6.32$ eV and 4.5 eV. The PDOS for the electronic ground state within GGA+U is presented in Fig. 3(c).

Fig. 3(c) shows the PDOS for C-AFM configuration calculated using GGA+U. The Eu- $4f$, Mn- $3d$, and Bi- p states are shifted farther from the Fermi level (E_F), exhibiting increased localization compared to GGA, and the band gap expands to approximately 0.258 eV within GGA+U. The similarity of the up- and down-spin components in both the valence bands (VBs) and conduction bands (CBs) for the

Table 3

The primitive coordinates (k_x, k_y, k_z) of two pairs of Weyl points (WPs) in the Brillouin zone (BZ) for EuMn_2Bi_2 in the C-AFM configuration are presented along with their corresponding energy (E) and chirality (C). The relative energies (E) of the WPs are given with respect to the Fermi level.

S. No.	k_x (\AA^{-1})	k_y (\AA^{-1})	k_z (\AA^{-1})	E_{gap} (eV)	E (eV)	Chirality (C)
1	0	0	0.03366	0	0.018	1
2	0	0	0.03341	0	0.018	-1
3	0	0	-0.03341	0	0.018	1
4	0	0	-0.03368	0	0.018	-1

GGA+ U electronic ground state suggests that the compound exhibits antiferromagnetic ordering.

Next, we calculated the band structure using both GGA and GGA+ U methods. Fig. 3(b) illustrates the band structure for the electronic ground state (G-AFM) within GGA, plotted along high-symmetry directions. In this Fig., a few bands intersect the Fermi level (E_F) without spin crossings, indicating a semimetallic nature with no discernible band gap. Additionally, the f orbitals appear localized near E_F , approximately at 0.5 eV. Fig. 3(d) shows the band structure for the C-AFM electronic ground state within GGA+ U . It is evident that no bands intersect E_F , and the band gap increases with larger U values for Eu. Furthermore, the f states are shifted approximately 1.75–2.5 eV below E_F . Within GGA+ U , the calculated band gaps are 0.122 eV and 0.258 eV for different U values, as listed in Table 2, indicating a semiconducting nature with a direct band gap along the Γ direction. Such AFM semiconducting behavior has also been reported for related layered pnictides such as EuMnBi_2 and EuCd_2As_2 [47, 48]. Fig. 4(b) presents the band structure for the C-AFM electronic ground state within GGA+ U +SOC. Here, the band touching at E_F along the Γ – A direction. Thus, 4.4 meV band gap is observed when SOC is included.

3.3. Topological properties

The total energy calculation place C-AFM and G-AFM states nearly degenerate, with an energy difference of only 6 meV/f.u. Choudhury *et al.* [19] have reported the G-AFM configuration to host a Dirac semimetal state. Therefore, in this section, we focus on the topological properties of the C-AFM configuration, which is marginally lower in energy and thus represent the most stable ground state. Topological states can often be identified by the presence of an inverted band structure arising from strong spin–orbit coupling (SOC) or crystal field effects [49, 21]. To examine this, we analyzed the bulk band structure and band symmetries of EuMn_2Bi_2 with and without SOC. As shown in Fig. 3(d), the C-AFM ground state exhibits an direct band

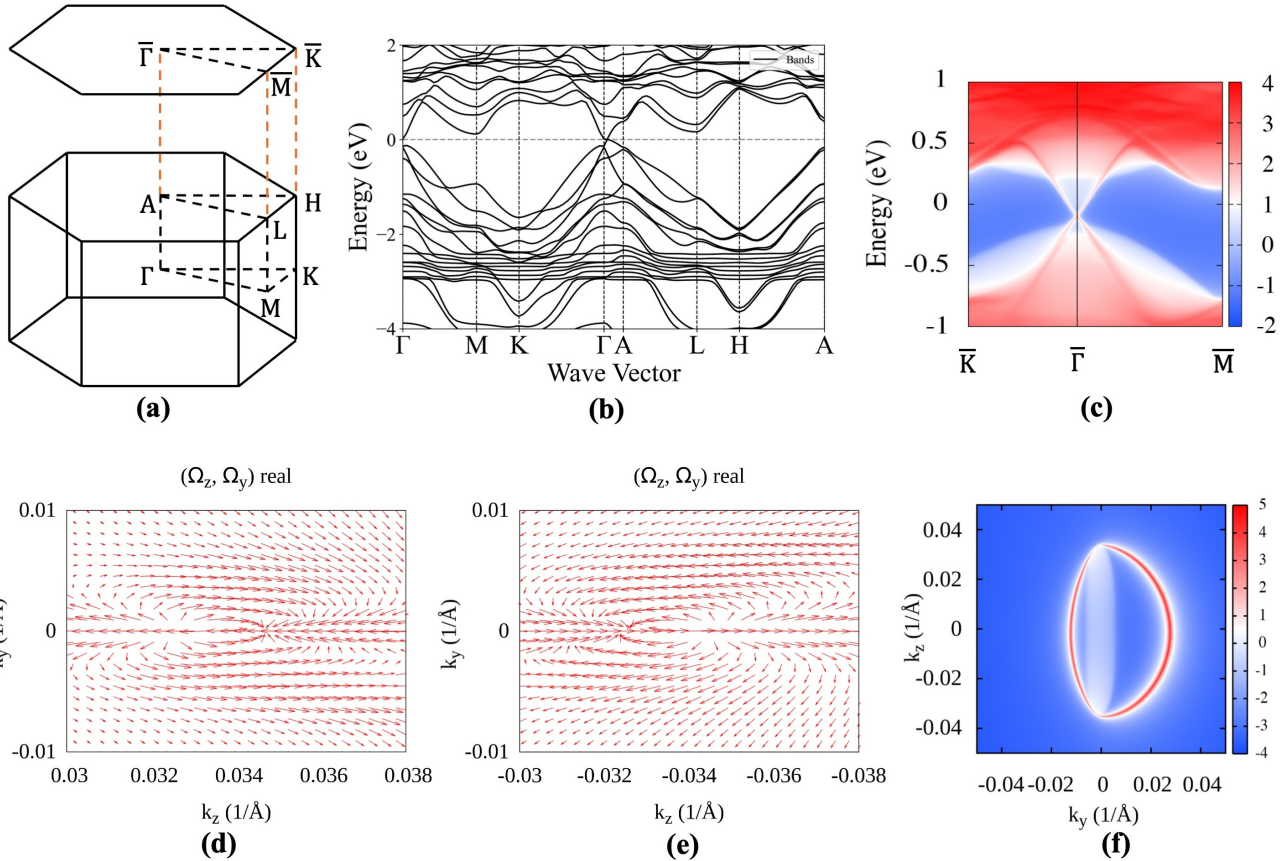


Figure 4: (a) Bulk Brillouin zone (BZ) and the corresponding (001) surface-projected BZ with high-symmetry points indicated. (b) Bulk electronic band structure of EuMn₂Bi₂ within SOC. (c) Surface spectral function of the (001) slab calculated along the \bar{K} - $\bar{\Gamma}$ - \bar{M} direction. Berry curvature distribution around (d) WPs 1 and 2, and (e) WPs 3 and 4 (as listed in Table 3), showing the characteristic monopole-like source and sink patterns associated with opposite chiralities. (f) The surface-projected Fermi arcs that connect WPs of opposite chirality.

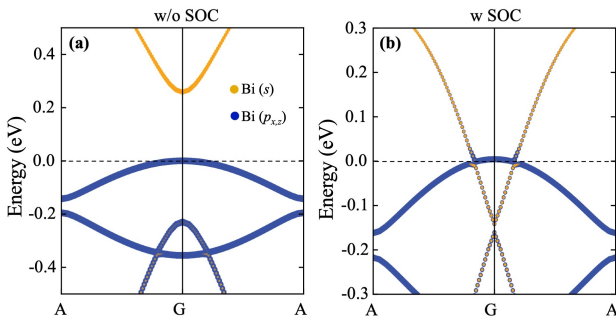


Figure 5: The band structures calculated (a) without and (b) with SOC, respectively. The projected contributions from the Bi s and $p_{x,z}$ orbitals are also displayed.

gap of 0.258 eV near the E_F , indicating that the system behaves as an antiferromagnetic semiconductor.

Because heavy orbitals such as Eu (4f), Mn (3d) and Bi (6p) are present, the effect of SOC is expected to be significant. When SOC is included in the C-AFM state, the

band gap decrease to 4.4 meV and CBs band and VBs touch the E_F along the Γ -A high-symmetry direction. This marks a topological phase transition from a trivial AFM semiconductor to a *Weyl semimetal (WSM)*. A closer examination of the calculated band structures along the A-G-A high-symmetry path shows the evolution of the electronic states near the E_F without and with SOC. In the absence of SOC [Fig. 5(a)], the Bi $p_{x,z}$ valence bands overlap near the E_F , while the Bi s conduction band lies slightly above it. Upon inclusion of SOC, the relative ordering of these states is significantly modified, as the Bi s band and the Bi $p_{x,z}$ bands cross the E_F , undergo a pronounced band inversion, and consequently reduce the band gap, as shown in Fig. 5(b). This SOC-driven reordering of orbital characters is consistent with the SOC-induced orbital inversion mechanisms discussed by Zhang *et al.* [50]. A detailed search of the band structure found four symmetry-related Weyl points (WPs) located at (0, 0, 0.03366) and (0, 0, 0.03341), with corresponding symmetry-related-points at (0, 0, -0.03366) and (0, 0, 0.03341), each WPs has a topological charge such as chirality $C = \pm 1$, present in Table 3. In this compound

the coexistence of inversion symmetry (\mathcal{P}) and broken time-reversal symmetry (\mathcal{T}) enforces the Weyl points to appear in $\pm\mathbf{k}$ pairs with opposite chirality, resulting in a net zero Chern number as required by the fermion doubling theorem [49, 21].

To elucidate their topological nature, we calculated the Berry curvature $\Omega(\mathbf{k})$ throughout the BZ. The Berry curvature field around the WPs exhibits monopole-like behaviour, acting as a *source* at the +1 chirality nodes and a *sink* at the -1 chirality nodes as shown in Figs. 4(d)-(e). Such Berry curvature hotspots are the origin of many exotic transport responses in WSMs, including the intrinsic anomalous Hall effect and chiral anomaly [49, 20]. The topological character is further explored by the surface electronic structure. As shown in Fig. 4(c), the surface spectral function of a (001) slab along the $\bar{K}-\bar{\Gamma}-\bar{M}$ path shows gapless surface states terminating at the projected bulk Weyl points. Moreover, a constant-energy contour at $E = E_F$ reveals open two Fermi arcs connecting each pair of the surface projections of WPs with opposite chirality [see Fig. 4(f)]. These Fermi arcs are a hallmark of EuMn_2Bi_2 compound and has a Weyl semimetals and similar features have been reported in other magnetic WSMs such as EuCd_2Bi_2 , and $\text{Co}_3\text{Sn}_2\text{S}_2$ [20, 21]. Moreover, the topological characteristics of EuMn_2Bi_2 can be placed in the broader context of magnetism-driven topological phases that have been extensively reported in layered magnetic materials. In particular, recent studies on MnBi_2Te_4 and related compounds have demonstrated that intrinsic antiferromagnetic order, layer-dependent magnetism, and strong spin-orbit coupling can generate axion insulator states, quantum anomalous Hall phases, and tunable Weyl band topology [51, 52, 53, 54, 55, 56]. These investigations collectively underscore how band inversion, surface-state gap formation, and Berry-curvature engineering are highly sensitive to magnetic configuration and chemical composition, thereby supporting the observed topological tunability in EuMn_2Bi_2 .

3.4. Electronic and magnetic properties of $\text{EuMn}X\text{Bi}_2$

The electronic and magnetic properties of $\text{EuMn}X\text{Bi}_2$ ($X = \text{Fe, Co, and Zn}$) were investigated using the GGA+ U and GGA+ U +SOC approaches. Owing to the strong electronic correlations associated with the Eu-*f*, Mn-*d*, Fe-*d*, and Co-*d* orbitals, the GGA+ U scheme was adopted, with the effective Hubbard parameters (U_{eff}) determined using the LR approach [28] (Table 4). The parent compound EuMn_2Bi_2 crystallizes in the trigonal CaAl_2Si_2 -type structure (space group $P\bar{3}m1$). To examine substitutional effects, one Mn atom was replaced by Fe, Co, or Zn, and the corresponding ground-state energies were computed (Table 4).

For EuMnFeBi_2 , the lowest-energy configuration is a C-AFM state, lying substantially below the FM, A-AFM, and G-AFM configurations, with $\Delta E = E_{\text{AFM}} - E_{\text{FM}} = -0.31$ eV. The density of states (DOS) reveals highly localized Fe-*d* and Bi-*p* states near the Fermi level (E_F),

Table 4

Calculated Hubbard parameters U_{eff} (eV), total energies (eV) of $\text{EuMn}X\text{Bi}_2$ for FM and three AFM configurations within GGA+ U , energy differences $\Delta E = E_{\text{AFM}} - E_{\text{FM}}$ (eV), and magnetic moments (μ_B /atom).

	EuMnFeBi_2	EuMnCoBi_2	EuMnZnBi_2
U_{eff} (Eu)	7.20	5.25	6.20
U_{eff} (Mn)	5.00	3.37	4.68
U_{eff} (Fe, Co)	4.00	4.82	—
FM	-61.14	-59.16	-54.11
A-AFM	-61.16	-59.11	-54.08
C-AFM	-61.45	-59.46	—
G-AFM	-61.32	-59.39	—
ΔE	-0.31	-0.30	0.02
μ_{Eu}	7.024	6.971	7.00
μ_{Mn}	4.575	4.437	4.595
μ_{Fe}	3.326	—	—
μ_{Co}	—	2.160	—

while the Eu-*f*, Mn-*d*, and Bi-*s* states are more delocalized and cross E_F [Fig. 6(a)]. The unequal spin distribution indicates a ferrimagnetic (FiM) ground state, with calculated magnetic moments of $\pm 7.024 \mu_B/\text{Eu}$, $\pm 4.575 \mu_B/\text{Mn}$, and $\pm 3.326 \mu_B/\text{Fe}$, yielding a net moment of $1.016 \mu_B/\text{f.u.}$ The band structure within GGA+ U [Fig. 6(b)] shows multiple conduction bands (CBs) crossing E_F at the Γ , K-M, A, and L k -points, with no valence bands (VBs) intersecting E_F , confirming a semimetallic nature. In the C-AFM state with SOC [Fig. 6(c)], several CBs intersect E_F and some VBs touch or cross E_F , eliminating the gap. The orbital states broaden above and below E_F , confirming that EuMnFeBi_2 adopts a ferrimagnetic semimetallic ground state.

Similarly, EuMnCoBi_2 stabilizes in a C-AFM configuration with $\Delta E = E_{\text{AFM}} - E_{\text{FM}} = -0.30$ eV. The DOS indicates pronounced Co-*d*, and Bi-*p* localization near E_F , while the Eu-*f*, Mn-*d*, and Bi-*s* states are delocalized [Fig. 6(e)]. The unequal spin polarization indicates FiM ordering, with magnetic moments of $\pm 6.971 \mu_B/\text{Eu}$, $\pm 4.437 \mu_B/\text{Mn}$, and $\pm 2.160 \mu_B/\text{Co}$, giving a total moment of $2.025 \mu_B/\text{f.u.}$, larger than that of EuMnFeBi_2 . The band structure for the C-AFM state within GGA+ U [Fig. 6(f)] shows four CBs intersecting E_F at Γ , K-M, A, and L k -points without spin crossings, while no VBs intersect E_F , confirming its semimetallic nature. The Eu-*f* orbitals are more delocalized, lying between 2.5 and 3 eV, and exhibit spin asymmetry between the spin-up and spin-down channels. In the presence of SOC [Fig. 6(g)], several CBs and some VBs cross or touch E_F , removing the band gap. The broadened orbital states above and below E_F confirm that EuMnCoBi_2 also exhibits a ferrimagnetic semimetallic character.

In contrast, EuMnZnBi_2 favors a FM ground state within GGA+ U , as the energy difference $\Delta E = E_{\text{AFM}} - E_{\text{FM}} = 0.02$ eV is negligible. The DOS shows weak localization of the Eu-*f*, Mn-*d*, Zn-*s*, and Bi-*p* states near E_F , and the unequal spin polarization confirms FM ordering [Fig. 6(i)].

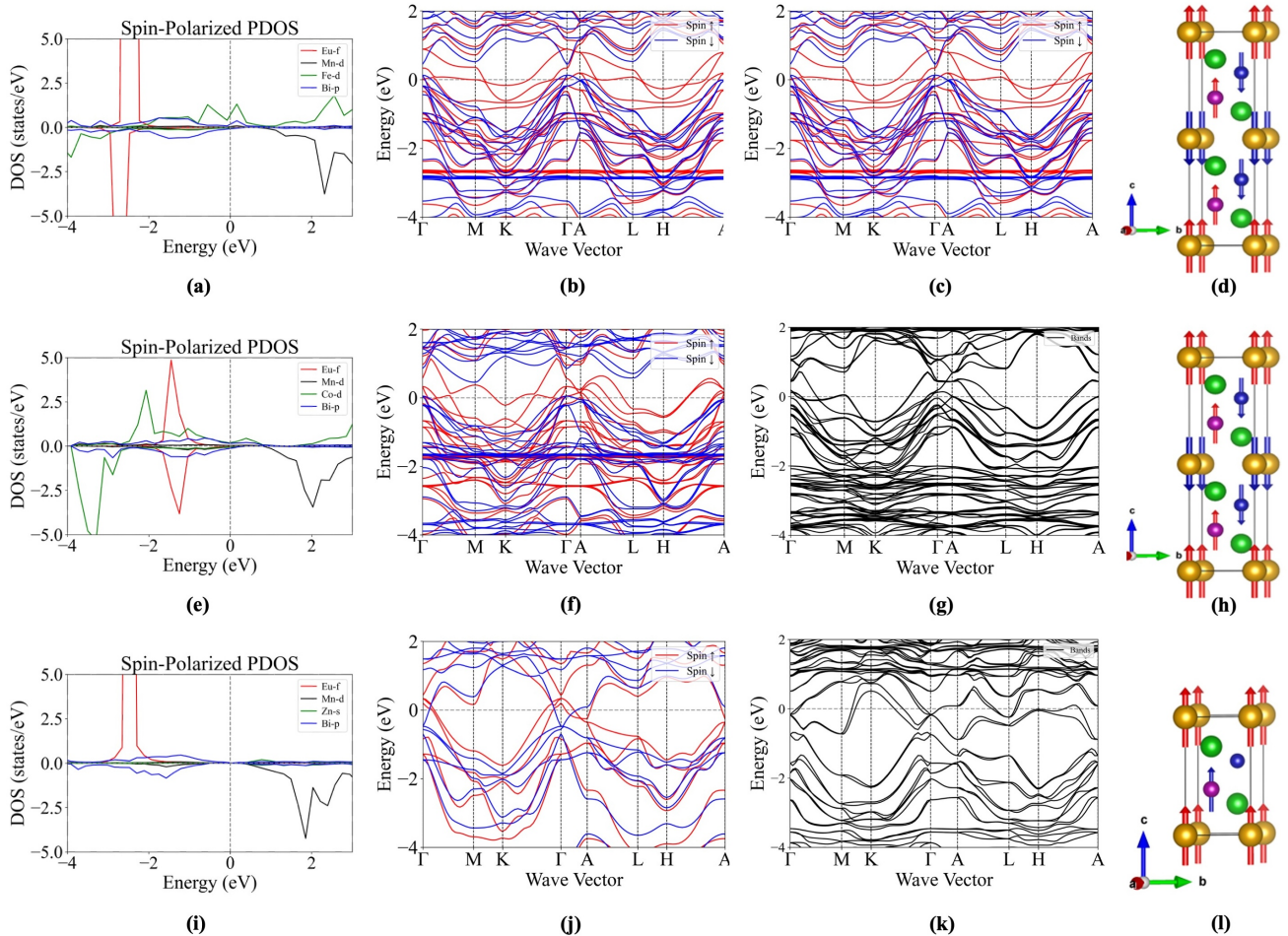


Figure 6: Spin-polarized projected density of state (PDOS), band structure, and crystal structure for magnetic ground state of the EuMnXBi_2 ($\text{X} = \text{Fe, Co, and Zn}$). (a)-(d) PDOS, band structure, and magnetic crystal structure of EuMnFeBi_2 . (a)-(b) PDOS, along with the band structure for the C-AFM ground state within the GGA+U framework. (c) band structure for the C-AFM ground state incorporating GGA+U+SOC. (d) C-AFM crystal structure, with blue representing Fe atoms. Similarly, (e)-(h) PDOS, band structure, and magnetic crystal structure of EuMnCoBi_2 . (e)-(f) PDOS, along with the band structure for the C-AFM ground state within the GGA+U framework. (g) band structure for the C-AFM ground state incorporating GGA+U+SOC. (h) C-AFM crystal structure, with blue representing Co atoms. Finally, (i)-(l) PDOS, band structure, and magnetic crystal structure of EuMnZnBi_2 . (i)-(j) PDOS, along with the band structure for the FM ground state within the GGA+U framework. (k) band structure for the FM ground state incorporating GGA+U+SOC. (l) FM crystal structure, with blue representing Zn atoms.

The calculated magnetic moments are $\pm 7.00 \mu_B/\text{Eu}$ and $\pm 4.595 \mu_B/\text{Mn}$, producing a large net moment of $11.497 \mu_B/\text{f.u.}$, consistent with ferromagnetism. The band structure [Fig. 6(j)] shows multiple CBs and VBs crossing E_F at the Γ and A k -points without spin crossings, indicating semimetallic behavior. With SOC [Fig. 6(k)], both CBs and VBs broaden and touch E_F , closing the gap and confirming its ferromagnetic semimetallic character.

To understand the origin of the distinct magnetic ground states in the substituted compounds, we analyzed the spin-polarized PDOS and orbital-resolved band structures of EuMnXBi_2 ($\text{X} = \text{Fe, Co, Zn}$), as shown in Fig. 6, together with the total-energy data in Table 4. The parent compound EuMn_2Bi_2 lies extremely close to a magnetic

phase boundary, because the energy difference between C-AFM and G-AFM configurations is only a 6 meV, indicating strong magnetic near-degeneracy. As a result, chemical substitution readily breaks this delicate balance by altering the Mn–Bi–Mn super-exchange pathways and the local Mn-3d electronic environment, making doping an efficient tuning parameter. For EuMnFeBi_2 and EuMnCoBi_2 , the Fe/Co 3d states are partially occupied and carry sizable local moments of about 3.33 and 2.16 μ_B , respectively, which couple antiparallel to the Mn moments ($\sim 4.5 \mu_B$), yielding a ferrimagnetic alignment within the Mn–X sublattice. The PDOS in Figs. 6(a) and 6(e) reveals strong hybridization between Fe/Co 3d and Bi p states near the E_F , favoring antiferromagnetic Mn–X superexchange in accordance with the Goodenough–Kanamori rules [57, 58]. Consistently, the

C–AFM configuration is about 0.30–0.31 eV per formula unit lower in energy than the FM state for X = Fe and Co (Table 4), demonstrating that the parent compound's near-degenerate AFM manifold is decisively tipped toward a ferrimagnetic ground state upon Fe or Co substitution.

In contrast, in EuMnZnBi₂ the Zn 4s orbitals contribute only weakly near the E_F [Fig. 6(i)], and Zn behaves as an almost nonmagnetic spacer. Here the doping effect is predominantly electronic: Zn substitution introduces additional electrons into the Mn–Bi network and shifts the Bi p states closer to the E_F [Figs. 6(j) and 6(k)]. This enhances the itinerant Bi- p -mediated Mn–Mn ferromagnetic exchange, analogous to the electron-induced interlayer ferromagnetism reported in MnBi₂Te₄ [59]. Consequently, EuMnZnBi₂ stabilizes a ferromagnetic ground state with a small positive energy difference, $\Delta E = E_{\text{AFM}} - E_{\text{FM}} \approx 0.02$ eV, highlighting how the parent compound's magnetic near-degeneracy amplifies the system's sensitivity to electron doping and leads to qualitatively different magnetic behavior for Fe/Co versus Zn substitution.

In summary, substitution of Mn by Fe or Co stabilizes ferrimagnetic ground states with semimetallic behavior, while Zn substitution drives the system into a ferromagnetic semimetallic state with a large net moment. These results demonstrate that transition-metal substitution in EuMn₂Bi₂ tunes the balance between AFM and FM exchange interactions, producing distinct magnetic ground states while retaining semimetallic character.

4. Conclusion

The structural, electronic, magnetic, and topological properties of EuMn₂Bi₂ using density functional theory (DFT) within the GGA+ U framework ($U_{\text{Eu}} = 6.32$ eV, $U_{\text{Mn}} = 4.16$ eV). EuMn₂Bi₂ crystallizes in the trigonal CaAl₂Si₂-type structure with space group $P\bar{3}m1$ (No. 164) and stabilizes in an antiferromagnetic ground state. The calculated magnetic moments are 6.98 μ_B /Eu for Eu²⁺ and 4.55 μ_B /Mn for Mn²⁺, consistent with previous experimental and theoretical results. The net magnetization is zero, consistent with AFM ordering. EuMn₂Bi₂ is classified as a narrow-gap semiconductor, with a direct band gap of 0.258 eV at the Γ point. The Eu- f orbitals remain highly localized and lie well below the Fermi level (E_F), while the spin-up and spin-down bands are nearly symmetric, reflecting the compensated AFM state. Elemental substitution of Mn by Fe, Co, and Zn was also explored: Fe and Co doping drives the system toward a ferrimagnetic (FiM) state, while Zn doping stabilizes a ferromagnetic (FM) state, and these substituted systems exhibit semimetallic characteristics. The Mn–X (X = Mn, Fe, Co, Zn) exchange interactions are found to evolve from antiferromagnetic to ferromagnetic upon substitution.

Furthermore, inclusion of SOC profoundly modifies the band topology of pristine EuMn₂Bi₂. SOC closes the band

gap in the antiferromagnetic state and induces band touching near the Fermi level, which in turn produces a band inversion between the Bi s and Bi $p_{x,z}$ orbitals along the $\Gamma - A$ direction, giving rise to topological features such as Dirac and Weyl fermions. Four symmetry-related Weyl points are observed near E_F , appearing in $\pm\mathbf{k}$ pairs with opposite chirality due to inversion symmetry, and they act as monopole-like sources and sinks of Berry curvature. The Berry curvature hotspots, gapless surface states, and surface-projected Fermi arcs provide clear evidence for the emergence of a magnetic Weyl semimetal phase in this system.

The coexistence of broken time-reversal symmetry and non-trivial band topology makes EuMn₂Bi₂ a promising candidate for topological spintronic applications. The Weyl fermions and their associated Berry curvature can enable efficient spin–charge interconversion, while the robust Fermi arc states can serve as scattering-immune spin-polarized transport channels. Overall, our findings highlight EuMn₂Bi₂ as a versatile platform for engineering correlated magnetic topological phases and developing next-generation spintronic devices.

References

- [1] Marcus Tegel, Marianne Rotter, Veronika Weiss, Falko M Schapacher, Rainer Pöttgen, and Dirk Johrendt. Structural and magnetic phase transitions in the ternary iron arsenides FeAs_2 and EuFe_2As_2 . *Journal of Physics: Condensed Matter*, 20(45):452201, 2008.
- [2] GR Stewart. Superconductivity in iron compounds. *Reviews of Modern Physics*, 83(4):1589–1652, 2011.
- [3] R Rühl and W Jeitschko. New pnictides with $\text{Ce}_2\text{O}_2\text{S}$ -type structure. *Materials Research Bulletin*, 14(4):513–517, 1979.
- [4] Sina Zapf and Martin Dressel. Europium-based iron pnictides: a unique laboratory for magnetism, superconductivity and structural effects. *Reports on Progress in Physics*, 80(1):016501, 2016.
- [5] CF Miclea, M Nicklas, Hirale S Jeevan, Deepa Kasinathan, Z Hosain, Helge Rosner, Philipp Gegenwart, Christoph Geibel, and Frank Steglich. Evidence for a reentrant superconducting state in EuFe_2As_2 under pressure. *Physical Review B—Condensed Matter and Materials Physics*, 79(21):212509, 2009.
- [6] Motoharu Imai, Hideki Abe, and Kei Yamada. Electrical properties of single-crystalline CaAl_2Si_2 . *Inorganic Chemistry*, 43(17):5186–5188, 2004.
- [7] Jyoti Krishna, Tashi Nautiyal, and Tulika Maitra. First-principles study of electronic structure, transport, and optical properties of EuCd_2 as 2. *Physical Review B*, 98(12):125110, 2018.
- [8] VK Anand and DC Johnston. Metallic behavior induced by potassium doping of the trigonal antiferromagnetic insulator EuMn_2Si_2 . *Physical Review B*, 94(1):014431, 2016.
- [9] JW Simonson, GJ Smith, K Post, M Pezzoli, JJ Kistner-Morris, DE McNally, JE Hassinger, CS Nelson, G Kotliar, DN Basov, et al. Magnetic and structural phase diagram of CaMn_2Si_2 . *Physical Review B—Condensed Matter and Materials Physics*, 86(18):184430, 2012.
- [10] Dimitri N Basov, Richard D Averitt, Dirk Van Der Marel, Martin Dressel, and Kristjan Haule. Electrodynamics of correlated electron materials. *Reviews of Modern Physics*, 83(2):471–541, 2011.
- [11] JW Simonson, K Post, C Marques, G Smith, O Khatib, DN Basov, and MC Aronson. Gap states in insulating LaMnPO_4 ($x = 0$ –0.3). *Physical Review B—Condensed Matter and Materials Physics*, 84(16):165129, 2011.
- [12] Abhishek Pandey, VK Anand, and DC Johnston. Large miscibility gap in the $\text{Ba}(\text{Mn}_x\text{Fe}_{1-x})_2$ system. *Physical Review B—Condensed Matter and Materials Physics*, 86(18):184430, 2012.

Matter and Materials Physics, 84(1):014405, 2011.

[13] A Dahal, Yiyao Chen, T Heitmann, A Thamizhavel, U Paramanik, SK Dhar, and DK Singh. Spin correlation in trigonal eumn 2 as 2. *Physical Review B*, 99(8):085135, 2019.

[14] Amy C Payne, Angella E Sprauve, Marilyn M Olmstead, Susan M Kauzlarich, Julia Y Chan, BA Reisner, and JW Lynn. Synthesis, magnetic and electronic properties of single crystals of eumn2p2. *Journal of Solid State Chemistry*, 163(2):498–505, 2002.

[15] Tanya Berry, Nicodemos Varnava, Dominic H Ryan, Veronica J Stewart, Riho Rasta, Ivo Heinmaa, Nitesh Kumar, Walter Schnelle, Rishi Bhandia, Christopher M Pasco, et al. Bonding and suppression of a magnetic phase transition in eumn2p2. *Journal of the American Chemical Society*, 145(8):4527–4533, 2023.

[16] Inga Schellenberg, Matthias Eul, Wilfried Hermes, and Rainer Pöttgen. A 121sb and 151eu mössbauer spectroscopic investigation of eumn2sb2, euzn2sb2, ybmn2sb2, and ybzn2sb2, 2010.

[17] Karl A Gschneidner, Jean-Claude G Bünzli, and Vitalij K Pecharsky. *Handbook on the physics and chemistry of rare earths*, volume 34. Elsevier, 2004.

[18] Yogesh Khatri and Arti Kashyap. Advancing magnetic material discovery through machine learning: Unveiling new manganese-based materials. *APL Machine Learning*, 1(4), 2023.

[19] Amarjyoti Choudhury and T Maitra. Emerging topological states in eumn2bi2: A first principles prediction. *Computational Materials Science*, 242:113091, 2024.

[20] Hao Wang, Ning Mao, Xiangting Hu, Ying Dai, Baibiao Huang, and Chengwang Niu. A magnetic topological insulator in two-dimensional eucd 2 bi 2: giant gap with robust topology against magnetic transitions. *Materials Horizons*, 8(3):956–961, 2021.

[21] Davide Grassano, Luca Binci, and Nicola Marzari. Type-i antiferromagnetic weyl semimetal inmn2. *Physical Review Research*, 6(1):013140, 2024.

[22] Peter E Blöchl. Projector augmented-wave method. *Physical review B*, 50(24):17953, 1994.

[23] S López-Moreno, AH Romero, J Mejía-López, and A Muñoz. First-principles study of pressure-induced structural phase transitions in mnf2. *Physical Chemistry Chemical Physics*, 18(48):33250–33263, 2016.

[24] Georg Kresse and Daniel Joubert. From ultrasoft pseudopotentials to the projector augmented-wave method. *Physical review b*, 59(3):1758, 1999.

[25] James D Pack and Hendrik J Monkhorst. " special points for brillouin-zone integrations"—a reply. *Physical Review B*, 16(4):1748, 1977.

[26] Martin Schlipf, Markus Betzinger, Marjana Ležaić, Christoph Friedrich, and Stefan Blügel. Structural, electronic, and magnetic properties of the europium chalcogenides: A hybrid-functional dft study. *Physical Review B—Condensed Matter and Materials Physics*, 88(9):094433, 2013.

[27] Wei Chen, Qi Chen, Jianming Zhang, Lin Zhou, Wenxiao Tang, Zhiyou Wang, Jiwei Deng, and Shifeng Wang. Electronic and magnetic properties of transition-metal-doped monolayer b2 s2 within gga+u framework. *RSC advances*, 14(5):3390–3399, 2024.

[28] Matteo Cococcioni and Stefano De Gironcoli. Linear response approach to the calculation of the effective interaction parameters in the lda+ u method. *Physical Review B—Condensed Matter and Materials Physics*, 71(3):035105, 2005.

[29] Hong TT Nguyen, Vo TT Vi, Tuan V Vu, Nguyen V Hieu, Dung V Lu, DP Rai, and Nguyen TT Binh. Spin-orbit coupling effect on electronic, optical, and thermoelectric properties of janus ga 2 sse. *RSC advances*, 10(73):44785–44792, 2020.

[30] Arash A Mostofi, Jonathan R Yates, Giovanni Pizzi, Young-Su Lee, Ivo Souza, David Vanderbilt, and Nicola Marzari. An updated version of wannier90: A tool for obtaining maximally-localised wannier functions. *Computer Physics Communications*, 185(8):2309–2310, 2014.

[31] Nicola Marzari, Arash A Mostofi, Jonathan R Yates, Ivo Souza, and David Vanderbilt. Maximally localized wannier functions: Theory and applications. *Reviews of Modern Physics*, 84(4):1419–1475, 2012.

[32] QuanSheng Wu, ShengNan Zhang, Hai-Feng Song, Matthias Troyer, and Alexey A Soluyanov. Wanniertools: An open-source software package for novel topological materials. *Computer Physics Communications*, 224:405–416, 2018.

[33] John MD Coey. *Magnetism and magnetic materials*. Cambridge university press, 2010.

[34] Sufyan Naji, Adil Belhaj, Hicham Labrim, Mohamed Bhihi, Abdellah Benyoussef, and Abdallah El Kenz. Electronic and magnetic properties of iron adsorption on graphene with double hexagonal geometry. *International Journal of Quantum Chemistry*, 114(7):463–467, 2014.

[35] S Naji, A Belhaj, H Labrim, M Bhihi, A Benyoussef, and A El Kenz. Adsorption of co and ni on graphene with a double hexagonal symmetry: electronic and magnetic properties. *The Journal of Physical Chemistry C*, 118(9):4924–4929, 2014.

[36] F El Hallani, S Naji, H Ez-Zahraouy, and A Benyoussef. First-principles study of the magnetic stability and the exchange couplings of lamn2o5. *Journal of Applied Physics*, 114(16), 2013.

[37] Burak Hımmetoglu, Andrea Floris, Stefano De Gironcoli, and Matteo Cococcioni. Hubbard-corrected dft energy functionals: The lda+ u description of correlated systems. *International Journal of Quantum Chemistry*, 114(1):14–49, 2014.

[38] Ruchika Mahajan, Iurii Timrov, Nicola Marzari, and Arti Kashyap. Importance of intersite hubbard interactions in β -mno 2: A first-principles dft+ u+ v study. *Physical Review Materials*, 5(10):104402, 2021.

[39] Runhan Li, Hao Wang, Ning Mao, Hongkai Ma, Baibiao Huang, Ying Dai, and Chengwang Niu. Engineering antiferromagnetic topological insulator by strain in two-dimensional rare-earth pnictide eucd2sb2. *Applied Physics Letters*, 119(17), 2021.

[40] Roderich Moessner and Arthur P Ramirez. Geometrical frustration. *Physics Today*, 59(2):24–29, 2006.

[41] Igor Žutić, Jaroslav Fabian, and S Das Sarma. Spintronics: Fundamentals and applications. *Reviews of modern physics*, 76(2):323, 2004.

[42] Kateryna Foyevtsova, Harald O Jeschke, II Mazin, DI Khomskii, and Roser Valentí. Ab initio analysis of the tight-binding parameters and magnetic interactions in na 2 iro 3. *Physical Review B—Condensed Matter and Materials Physics*, 88(3):035107, 2013.

[43] Jeffrey G Rau, Eric Kin-Ho Lee, and Hae-Young Kee. Spin-orbit physics giving rise to novel phases in correlated systems: Iridates and related materials. *Annual Review of Condensed Matter Physics*, 7(1):195–221, 2016.

[44] Yogesh Khatri, Ralph Skomski, Wenyong Zhang, Shah R Vallappilly, David J Sellmyer, and Arti Kashyap. Magnetic and structural properties of mnxn3 (x= mn, fe, co). *AIP Advances*, 11(1), 2021.

[45] Jan Rusz, Lars Bergqvist, J Kudrnovský, and Ilja Turek. Exchange interactions and curie temperatures in ni 2- x mn sb alloys: First-principles study. *Physical Review B—Condensed Matter and Materials Physics*, 73(21):214412, 2006.

[46] Hung Ba Tran and Hao Li. Realistic finite temperature simulations for the magnetic and transport properties of ferromagnets. *Journal of Materials Chemistry C*, 13(22):11393–11401, 2025.

[47] Hidetoshi Masuda, Hideaki Sakai, Masashi Tokunaga, Yuichi Yamasaki, Atsushi Miyake, Junichi Shiogai, Shintaro Nakamura, Satoshi Awaji, Atsushi Tsukazaki, Hironori Nakao, et al. Quantum hall effect in a bulk antiferromagnet eumnb2 with magnetically confined two-dimensional dirac fermions. *Science advances*, 2(1):e1501117, 2016.

[48] Marein C Rahn, J-R Soh, S Francoual, LSI Veiga, J Strempfer, J Mardegan, DY Yan, YF Guo, YG Shi, and AT Boothroyd. Coupling of magnetic order and charge transport in the candidate dirac semimetal eucd 2 as 2. *Physical Review B*, 97(21):214422, 2018.

[49] N Peter Armitage, Eugene J Mele, and Ashvin Vishwanath. Weyl and dirac semimetals in three-dimensional solids. *Reviews of Modern Physics*, 90(1):015001, 2018.

[50] Huisheng Zhang, Yingying Wang, Wenjia Yang, Jingjing Zhang, Xiaohong Xu, and Feng Liu. Selective substrate-orbital-filtering

effect to realize the large-gap quantum spin hall effect. *Nano Letters*, 21(13):5828–5833, 2021.

[51] Chang Liu, Yongchao Wang, Hao Li, Yang Wu, Yaoxin Li, Jiaheng Li, Ke He, Yong Xu, Jinsong Zhang, and Yayu Wang. Robust axion insulator and chern insulator phases in a two-dimensional antiferromagnetic topological insulator. *Nature materials*, 19(5):522–527, 2020.

[52] Yujun Deng, Yijun Yu, Meng Zhu Shi, Zhongxun Guo, Zihan Xu, Jing Wang, Xian Hui Chen, and Yuanbo Zhang. Quantum anomalous hall effect in intrinsic magnetic topological insulator mnbi2te4. *Science*, 367(6480):895–900, 2020.

[53] Jiaheng Li, Yang Li, Shiqiao Du, Zun Wang, Bing-Lin Gu, Shou-Cheng Zhang, Ke He, Wenhui Duan, and Yong Xu. Intrinsic magnetic topological insulators in van der waals layered mnbi2te4-family materials. *Science advances*, 5(6):eaaw5685, 2019.

[54] Dongqin Zhang, Minji Shi, Tongshuai Zhu, Dingyu Xing, Haijun Zhang, and Jing Wang. Topological axion states in the magnetic insulator mnbi 2 te 4 with the quantized magnetoelectric effect. *Physical review letters*, 122(20):206401, 2019.

[55] Huiheng Zhang, Wenjia Yang, Yingying Wang, and Xiaohong Xu. Tunable topological states in layered magnetic materials of mn sb 2 te 4, mn bi 2 se 4, and mn sb 2 se 4. *Physical Review B*, 103(9):094433, 2021.

[56] Huiheng Zhang, Wenjia Yang, Yaohui Ning, and Xiaohong Xu. Abundant valley-polarized states in two-dimensional ferromagnetic van der waals heterostructures. *Physical Review B*, 101(20):205404, 2020.

[57] John B Goodenough. An interpretation of the magnetic properties of the perovskite-type mixed crystals $La_{1-x}Sr_xCoO_3 - \lambda$. *Journal of Physics and chemistry of Solids*, 6(2-3):287–297, 1958.

[58] Junjiro Kanamori. Superexchange interaction and symmetry properties of electron orbitals. *Journal of Physics and Chemistry of Solids*, 10(2-3):87–98, 1959.

[59] Huiheng Zhang, Jiahui Peng, Yaling Zhang, Wenjia Yang, Yushuai Wang, Xiaoxiao Man, and Xiaohong Xu. Electron doping: A generic approach for realizing interlayer ferromagnetic coupling in the anti-ferromagnetic mnbi2te4 family of materials. *Physical Review B*, 111(1):014404, 2025.